Effect of pre-corrosion on damage evolution and crack propagation in aluminum alloy 7050-T7651

Effect of pre-corrosion on damage evolution and crack propagation in aluminum alloy 7050-T7651

Haipeng Song[a,b,*], Zhengguan Bai[a], Hao Zhang[c], Yifan Niu[a], Sean B. Leen[b]

[a] *Sino-European Institute of Aviation Engineering, Civil Aviation University of China, PR China*
[b] *Mechanical Engineering, College of Engineering and Informatics, NUI Galway, Ireland*
[c] *Department of Materials Engineering, KU Leuven, Belgium*

Abstract

This paper investigates the effects of pre-corrosion on the tensile behavior of aluminum alloy 7050-T7651. A combined experimental approach involving digital image correlation, scanning electron microscopy and tensile testing is presented for quantitative and qualitative analysis. A tensile damage model is presented for plasticity-induced, post-corrosion mechanical damage for interpretation and identification of damage-cracking thresholds. Although multiple corrosion-induced cracks evolve simultaneously in diffuse regions, propagation and coalescence of the main cracks, originating from key damage regions, dominate the failure process. A combined corrosion and mechanical damage model was used to successfully predict the effects of pre-corrosion on the tensile stress-strain response.

Keywords: Aluminum alloy; Localized corrosion; Damage evolution; Crack propagation; Digital image correlation

[*] Corresponding author.

E-mail address: haipeng.song@nuigalway.ie (Haipeng Song).

NOMENCLATURE

D	=	Damage
D_{cor}	=	Corrosion damage
D_{mech}	=	Mechanical damage
D_{total}	=	Total damage
E	=	Elasticity modulus
$\tilde{E}$	=	Apparent elasticity modulus of pre-corroded material
Q, b	=	Hardening parameters
$\tilde{Q}$	=	Apparent hardening parameter of pre-corroded material
S	=	Area of a section of the volume element
S_D	=	Total area of the section of all microcracks and micro-voids in *S*
$a_1, x_1, y_1, a_2, x_2, y_2$	=	Damage model parameters
d	=	Depth of corrosion pit
t	=	Pre-corrosion exposure time
σ	=	Stress
σ_u	=	Ultimate stress
σ_y	=	Flow stress
σ_{y0}	=	Initial yield stress
ε	=	Strain
ε_p	=	Plastic strain
ε_{pD}	=	Damage threshold plasic strain
ε_C	=	Threshold tensile strain of cracking
ε_D	=	Threshold tensile strain of damage
ε_u	=	Ultimate strain
α, β	=	Calibration parameters in pit growth model
k_1, k_2, k_3	=	Calibration parameters in corrosion-affected mechanical response model

1. INTRODUCTION

Aeronautic aluminum alloys such as 2xxx and 7xxx are widely used in fuselage frames, bulkheads and wing skins of aircrafts due to their high strength and light weight [1]. Unfortunately, these alloys are prone to localized corrosion, such as pitting corrosion and exfoliation corrosion, when exposed to corrosive environments during their service life [2, 3]. The corrosion-enhanced damage and cracking behavior in aluminum alloys adversely affects the performance of aircraft structure and even leads to component failures, which endangers the flight safety especially in aging aircrafts [4, 5]. In current aircraft structural integrity management, corrosion is typically removed on detection, due to the lack of a reliable methodology to predict the future effects of corrosion. This 'find and fix' policy is typically over-conservative since it temporarily removes otherwise serviceable aircraft from service for repair [4, 6]. Therefore, to improve methodologies of corrosion management, which will enable the continued safe, as well as economical, operation of aircraft, it is important to gain insight into the effects of localized corrosion on damage evolution and crack propagation in aluminum alloys.

As is well known, localized corrosion deteriorates the mechanical performance of aluminum alloys. Tensile tests conducted on pre-corroded 2024-T3 aluminum alloy showed that the ultimate tensile strength reduced by about 18 percent after 24 hours exposure in exfoliation corrosion (EXCO) solution [7], and fracture toughness exponentially decreased with increasing exposure time [8]. The presence of pre-existing localized corrosion also reduced the fatigue life of aluminum alloys by a factor ranging from 10 to 100 in comparison to that without corrosion [9-12]. Such mechanical property degradation is mainly attributed to the crack initiation and propagation derived from localized corrosion [13-17]. Fractographic analysis has shown that corrosion pitting caused accelerated crack initiation and promoted multiple-site damage cracks in aluminum alloy 2024-T3 under fatigue loading [18]. Three-dimensional X-ray micro tomographic images of steel in stress corrosion cracking have confirmed that cracks develop predominantly at the shoulder of the corrosion pit, near the pit-surface interface [19]. Interrupted tests were conducted on pre-corroded 2024-T3 aluminum alloy to investigate the crack initiation of corrosion-nucleated fatigue cracking. It was deduced that crack nucleation was essentially immediate upon the application of cyclic loading [20]. The effect of prior corrosion state on fatigue micro crack initiation and early stage propagation behavior of aluminum alloy 6151-T6 was investigated via in-situ scanning electron microscopy (SEM) tests, which indicated that multi-crack initiation occurred near the corrosion pits and the early stage of fatigue micro crack propagation behavior can be described by K_I-K_{II}-mixed mode [10]. The specimen surfaces were monitored by optical microscopy to investigate the short crack growth of pre-corroded 7075-T6 aluminum alloy. The results revealed that short crack growth life under salt water conditions was about 5 to 8 times lower than ambient air [21]. A crack surface marker-band method was used to determine the short crack growth rate of AA7050-T7451 samples with macro scale corrosion damage, crack growth rates were shown to converge to comparable values for varied corrosion morphologies [22].

Based on experimental observations, some modeling work was also conducted to discuss the damage evolution and crack propagation in metallic material with localized corrosion. A finite element (FE) analysis has been undertaken to evaluate the stress and strain distributions associated with a single

corrosion pit in a cylindrical steel specimen stressed remotely in tension, and it was shown that the plastic strain is localized on the pit walls below the pit mouth rather than at the pit base [23]. The stress distribution at semi elliptical corrosion pits in steel showed that aspect ratio is the main parameter affecting stress concentration factor [24]. A continuum damage mechanics model for corrosion-fatigue damage was presented to study the pit-to-crack initiation life in AA2024-T3 [25]. The model was based on the single dominant flaw approach, assuming that although several pits may be present; only one pit grows to a critical depth and transitions to a fatigue crack. Coupled elastic-plastic damage constitutive equations and elastic–plastic damage evolution models were adopted to predict the corrosion-fatigue life of aluminum alloy [2]. Linear elastic fracture mechanics modelling, using a corrosion modified-equivalent initial flaw size, was performed to predict the fatigue life of field corroded 7075-T6511 aluminum alloy under variable amplitude loading [15].

However, the effect of localized corrosion on the temporal and spatial characteristics of damage evolution and crack propagation in aluminum alloys remains unclear. It is difficult to achieve full-field damage evolution and crack propagation from fractographic analysis for macro-scale tests, especially for static loading condition. It is necessary to quantitatively observe the entire damage and failure process associated with increased load level using a full-field measurement technique, which can act as a bridge between loading curve data and fracture morphology. Among the different types of experimental methods, digital image correlation (DIC) is an effective method for obtaining the displacement and strain fields on the surface of materials, with the advantages of providing full-field, real-time, and non-contact measurements as well as flexibility [26, 27]. This optical technique has been extensively applied to various materials, such as metallic material [28-30], composite [31], and rock [32]. DIC was utilized to study the growth of multiple intergranular cracks as a colony on an Alloy 600 in a tetrathionate solution [33]. Short cracks during intergranular stress-corrosion cracking of austenitic stainless steel were detected by DIC [34]. The method was also used to monitor short fatigue crack propagation of austenitic stainless steel in oxygenated water [35]. The damage evolution in a macroscopic aluminum specimen with prior corrosion has not been studied with DIC for static or fatigue experiments. Besides, to better analyze and demarcate localized damage and crack initiation based on DIC strain maps, it is necessary to identify the threshold strains of damage and cracking, especially adopting the concepts of damage mechanics for ductile fracture [36, 37].

Considering that aircraft structures typically experience corrosion between flights and loading during flight [38], the present work focuses on quantifying the effect of ‘prior corrosion’ on damage evolution and crack propagation in aluminum alloy. The prior corrosion of aluminum alloy can be effectively simulated in laboratory via exposure in EXCO solution [5]. Uniaxial tension tests have been conducted on aluminum alloy specimens with different degrees of initial localized corrosion. Detailed analysis of damage evolution and crack propagation in specimens under different conditions is achieved with the combined use of DIC and SEM. The loading curves were recorded to reflect the degradation of macro-scale mechanical properties. Based on the mechanics of plasticity-induced damage [36, 37], threshold strain values of damage and cracking are identified. Then strain fields during the loading process are presented by DIC to describe the damage evolution and crack propagation of the material. The fracture morphology of key damage

regions determined by DIC is further examined to identify crack initiation and fracture features. Based on the experimental information, the effect of localized corrosion on damage evolution and crack propagation is discussed. A non-linear damage mechanics model, based on plasticity-induced damage, is developed and combined with pre-corrosion damage, based on the measured effects of pre-corrosion exposure time, to simulate the effect of pre-corrosion on the tensile response.

2. EXPERIMENT

2.1. Material and specimen

The aluminum alloy 7050-T7651 which is commonly used in critical aircraft structures is investigated in this work. The chemical composition (wt%) of the alloy is 0.01% Si, 0.09% Fe, 2.02% Cu, 0.01% Mn, 2.06% Mg, 0.01% Cr, 6.16% Zn, 0.03% Ti and Al remainder. The specimen preparation procedure are mechanical machining, pre-corrosion and painting. Firstly, the alloy was cut into dog-bone shaped specimens for uniaxial tension tests with the parallel region of 10×10 mm, and the thickness of 0.8 mm. The microstructure of specimen material is shown in Fig. 1. Secondly, to produce different levels of initial localized corrosion, three groups of specimens were exposed to EXCO solution (whole specimen) for 0, 4 and 6 hours respectively, according to specification ASTM G34-01 [39]. The corrosive solution consisted of the following chemicals diluted in 1L distilled water: sodium chloride (234 g NaCl), potassium nitrate (50 g KNO_3) and nitric acid (6.3 mL HNO_3). Fig. 2 displays typical corrosion states along the Long-Transverse (L-T) direction after exposure in EXCO resolution. Evident corrosion attack were observed on the surface after a duration of 4 hrs and became more extensive with increasing exposure time, indicating the severe detrimental impact of the corrosive solution on the aluminum alloy 7050-T7651. After corrosion exposure, all specimens were rinsed and ultrasonically cleaned for 15 minutes in ethyl alcohol, then dried. Finally, since the DIC method requires a contrasting random pattern on the surface of measured objects to identify surface deformation information, random speckle patterns were applied by spraying white and black paints on the surfaces of all specimens before loading.

2.3. Experimental set-up and procedure

Uniaxial tension tests were conducted on an Instron-5980 electric universal test machine in laboratory air at room temperature. Three groups of specimens was successively loaded in a displacement controlled mode with a loading speed of 0.1 mm/min. During the loading process, the surfaces of specimens were captured by a Charge-coupled Device (CCD) camera at an acquisition rate of 2 fps (frame per second). The resolution of the CCD capture region was 833×1446 pixels, and the length-pixel ratio of the imaging system was about 25.8 μm/pixel. After the tests, the acquired image sequences were processed using the commercial software VIC-2D (Correlated Solutions, Inc.), which determined the displacement fields in the DIC analysis region (shown in Fig. 3 (a)) by tracking the grey value pattern in small subsets throughout the image sequence. The subset size was chosen as 25 × 25 pixels, and the step length was 2 pixels. Then the displacement fields were numerically differentiated using the VIC-2D software to compute the surface strain tensor components.

3. RESULTS

3.1. Degradation of macro-scale mechanical properties

Typical stress-strain curves for the specimens with different levels of initial corrosion in the uniaxial tension tests are shown in Fig. 3 (b), which intuitively shows the influence of the prior corrosion on the macro-scale mechanical properties of the aluminum alloy. Table 1 shows the detailed mechanical parameters of specimens obtained from the stress-strain curves. It is clear that all of these properties degrade with increasing corrosion and the degree of degradation correlates with exposure time. As shown in Fig. 4 (a) and (b), stiffness (elasticity modulus), yield strength and ultimate tensile strength are all seen to degrade by similar amounts, approximately proportionally, to exposure duration, about 7% to 8% and 11% to 12% for 4 hrs and 6 hrs, respectively. Herein, the stiffness (elasticity modulus), yield strength and ultimate tensile strength should be understood as the apparent ones, since corrosion will reduce the initial section area of specimen, and the degradation of apparent properties could be considered as a function of specimen thickness. It is also revealed that corrosion has a detrimental effect on the ductility of the material, as shown in Fig. 4 (c). Rupture strain is detrimentally and significantly reduced by about 35% and 51%, respectively, which is also approximately proportional to corrosion duration. Ultimate strain also continuously decreased with the aggravation of initial corrosion damage, by about 24% to 30%. These experimental results clearly demonstrated that the presence of localized corrosion led to the degradation of apparent stiffness, strength and ductility of the material.

3.2. Identification of threshold strains and material parameters

To further analyze the effect of corrosion on mechanical response of material, and facilitate physical interpretation, analysis and demarcation of damage localization, crack initiation and propagation based on the DIC strain maps, it is useful to adopt the concepts of damage mechanics for ductile fracture. Lemaitre and Chaboche [36] have presented some fundamental concepts in damage mechanics for metallic materials. The damage variable D is defined based on the nucleation and growth of micro-voids and microcracks in a representative volume element:

$$D = \frac{S_D}{S} \tag{1}$$

where S is the area of a section of the volume element identified by its normal $\vec{n}$, and S_D is the total area of the section of all microcracks and micro-voids in S. In the case of uniaxial, isotropic, plastic deformation, the damage evolution can be described as follows:

$$D = \begin{cases} a_1 \left[1 - \dfrac{\left(\dfrac{\varepsilon_p}{\varepsilon_{pD}} \right)}{y_1} \right]^{x_1} + a_2 \left[1 - \dfrac{\left(\dfrac{\varepsilon_p}{\varepsilon_{pD}} \right)}{y_2} \right]^{x_2} & if\ \varepsilon_p > \varepsilon_{pD} \\ 0 & otherwise \end{cases} \tag{2}$$

in which ε_p represents the uniaxial plastic strain, and ε_{pD} is the damage threshold plastic strain, a_1, x_1, y_1, a_2, x_2, y_2 are the material parameters. It is commonly observed that the localized plastic deformation induced damage initiates when the tensile strain reaches the value corresponding to the ultimate stress σ_u [37]. This point was also corresponds to the start of necking in the literature [40-42]. However, the specimen thickness in this work was very thin, and the failed specimens and fracture surfaces shows negligible necking behavior; thus, the threshold tensile strain for damage ε_D is assumed here to be:

$$\varepsilon_D = \varepsilon_u \tag{3}$$

where σ_u is the ultimate stress, ε_u is the ultimate strain at $\sigma = \sigma_u$.

The threshold tensile strain for cracking ε_C is taken to be defined in term of the rupture tensile strain ε_R:

$$\varepsilon_C = \varepsilon_R \tag{4}$$

From our tests, the identified threshold tensile strains for damage initiation and cracking of aluminium alloy are shown in Fig. 5 and Table 2.

The hardening and damage parameters can also be identified by fitting the measured stress-strain curve of un-corroded specimen, which could be roughly divided into elastic, plastic, and soften stages as shown in Fig. 5. In the elastic stage, the relation of stress and strain is [36]

$$\sigma = E\varepsilon \tag{5}$$

in which σ represents tensile stress, ε is tensile strain and E is the elasticity modulus. From the initial yield point, the stress required to cause further plastic deformation increases, the flow stress can be written as [43]

$$\sigma_y(\varepsilon_p) = \sigma_{y0} + r(\varepsilon_p) \tag{6}$$

where σ_y is the flow stress, σ_{y0} is the initial yield stress, and $r(\varepsilon_p)$ is called the isotropic hardening function with the form as [36]

$$dr(\varepsilon_p) = b(Q - r)d\varepsilon_p \tag{7}$$

in which Q and b are hardening constants. After the peak point, damage causes the stress soften effect, gives

$$\sigma = \sigma_y(1 - D) \tag{8}$$

The calculated and measured stress-strain curves for the un-corroded specimen are shown in Fig. 5. Hardening parameters and damage parameters are given in Table 3.

3.3. Damage evolution and crack propagation by DIC

To reveal the details on damage evolution and crack propagation during the present uniaxial tension tests, maximum tensile strain fields of typical specimens at key tensile strain have been calculated via DIC. Based on the threshold values of strain for damage and cracking, we can distinguish strain localization, damage initiation, and cracking by comparing the local strain values to the threshold values of Table 2 (for 0h corrosion). For example, damage region could be identified when the local strain value locates between

damage threshold strain and cracking threshold strain. Crack could also be recognized when the local strain value reaches cracking threshold strain.

Fig. 6 shows the distributions of maximum tensile strain fields of the pristine specimen under five different deformation levels, denoted as A_1, B_1, C_1, D_1 and E_1. It is observed that deformation distribution is essentially uniform at the yield point (A_1 in Fig. 6, $\sigma = 445.7$ MPa). As the load increased to its peak value, some diffuse regions with strain values larger than damage threshold strain ε_D and smaller than the cracking threshold strain ε_C, designated here as 'diffuse damage' areas, appear in the middle of the specimen (B_1 in Fig. 6, $\sigma = 505.6$ MPa). This heterogeneous damage is gradually accentuated, accompanied by load reduction. Two regions, I_1 and I_2 marked with arrows, had larger strains than the cracking threshold strain ε_C, indicating micro-crack initiation in these two regions (C_1 in Fig. 6, $\sigma = 500.0$ MPa). With further damage evolution, the cracks in regions I_1 and I_2 propagated and joined with each other. Localized damage also led to further crack initiation in other regions, so that a belt-shaped zone formed along 45° direction (D_1 in Fig. 6, $\sigma = 473.8$ MPa). Finally, the unstable coalescence and propagation of these cracks resulted in final shear failure, as shown in Fig. 6 (E_1). The damage regions I_1 and I_2 played important roles in the damage evolution and failure process, and are referred to here as key damage regions (KDRs).

Fig. 7 presents the evolution of maximum tensile strain field corresponding to five tensile deformation levels A_2, B_2, C_2, D_2 and E_2 in the specimen with a corrosion time of 4 hrs. As for the no-corrosion case, no deformation localization is apparent at the yield point, which is about 8% lower in this case. The yield strain is almost equal to the no-corrosion case, i.e. 0.6%. (A_2 in Fig. 7, $\sigma = 408.3$ MPa). At the peak load, also reduced by ~8% relative to the no-corrosion case, localized damage regions with strain concentrations are evident (B_2 in Fig. 7). Compared to the no-corrosion specimen, there are more evident patterns of concentrated damage, apparently attributable to the pre-exiting localized corrosion damage. With further tensile deformation, these localized damage regions gradually enlarge and their degree of severity accordingly intensifies, leading to load reduction and increased localized strains to exceed the cracking threshold strain ε_C, indicating micro-crack nucleation in regions such as region II_1 indicated by the arrow (C_2 in Fig. 7, $\sigma = 458.8$ MPa). Subsequently, cracks in region II_1 propagated and joined with adjacent ones concomitant with further slight decline of load (D_2 in Fig. 7, $\sigma = 452.5$ MPa). Another micro-crack initiated in region II_2 at the same time. The propagation and coalescence of these two main cracks originated from KDRs II_1 and II_2, resulting in the catastrophic failure. Fig. 7 (E_2) shows the final failure mode, showing the obvious effect of KDRs II_1 and II_2 on the fracture path.

For the specimen with a corrosion duration of 6 hrs, the damage evolution associated with the five deformation levels is illustrated in Fig. 8. Two localized damage regions III_1 and III_2 are identified from the concentrated, large strains in the central part of the specimen at yield point (A_3 in Fig. 8, $\sigma = 396.6$ MPa). Compared to the specimen with an exposure time of 4 hrs, the more premature appearance of localized damage is attributed to more detrimental pre-existing localized corrosion. With the increasing load, damage regions I_3 and II_3 gradually grew and evolved in size and severity, leading to micro-crack initiation

when the load reached its maximum value (B_3 in Fig. 8, $\sigma = 445.9$ MPa). Further deformation, accompanied by slight load decrease, causes the cracks in region III_1 and III_2 to steadily propagate separately (C_3 in Fig. 8, $\sigma = 443.8$ MPa), and then coalesce (D_3 in Fig. 8, $\sigma = 437.5$ MPa). Although some micro-crack initiation is also observed in other locations, the cracks in KDRs III_1 and III_2 appear to be the dominant ones for final failure, as shown in Fig. 8 (E_3).

3.4. Fracture morphology of key damage regions

To further characterize and assess crack nucleation and failure microscale features, the fracture surfaces of the critical fracture regions of the specimens have been investigated via SEM, with specific focus on the KDRs identified by DIC. Fig. 9 (a) shows the fracture path of the un-corroded specimen of Fig. 6, showing KDRs I_1 and I_2. The fracture morphologies of region I_1 and I_2 are shown in Fig. 9 (b) and Fig. 9 (c), respectively. Crack initiation is observed at voids near the specimen surface and ductile striations are visible ahead of the propagating crack. The fracture surfaces also contained large regions of ductile dimples and micro-void coalescence, as shown in Fig. 9 (d). For the 4 hrs pre-corrosion case, Fig. 10 gives the fracture morphology of a failed specimen corresponding to Fig. 7. From the enlarged views of KDRs II_1 and II_2 show in Fig. 10 (b) and Fig. 10 (c), a cluster of corrosion pits is observed and it can be seen that cracks originated from the largest pit on the surface (darkened region as indicated by the arrow) in each key damage region. Furthermore, evidence of quasi-cleavage fracture regions is found, and noticeable material embrittlement features, induced by corrosion, are visible on the fracture surface, as shown in Fig. 10 (d). This is in agreement with the measured degradation of ductility from the loading curves. The localized corrosion that led to crack initiation in KDRs III_1 and III_2 for the 6 hrs corrosion specimen (Fig. 8) is shown in Fig. 11. The fracture morphologies are similar to those with 4 hrs exposure; cracks also initiated from the largest pit surrounded by a cluster of corrosion pits in each key damage region with some embrittlement features. The corrosion pits shown in Fig. 11 are generally larger than those in Fig. 10. In addition, inclusions were also found inside the material, as shown in Fig. 11 (d). It is noted that only three experiments were carried out in this paper, a broader range of experimental conditions need to be extended for a more robust generic conclusion on the damage mechanism.

Based on the discussion above, the size of the largest corrosion pit in key damage regions is a measure of the evolution of prior corrosion damage, which grows with increasing corrosion time. The relation between the corrosion pit depth and exposure duration can be described by the exponential function [44]:

$$d = \alpha t^{\beta} \tag{9}$$

in which d is the depth of corrosion pit, t is the corrosion exposure duration, α and β are fitting parameters. In this work, the depths were measured from the fracture morphology as shown in Fig. 9 and Fig. 10; and the corrosion pit growth function is identified as $d = 31.65t^{0.83}$.

3.5. Corrosion-enhanced damage and failure process

The corrosion-induced degradation in specimen mechanical properties observed in this work (Fig. 4) are larger in magnitude than obtained in tests of aluminum alloy 2024 reported by Pantelakis *et al* [7] and

Alexopoulos *et al* [8]. The apparent stiffness, strength and ductility are all seen to degrade approximately proportional to exposure duration, in contrast with previous work, for longer durations, where an exponential decrease with time was observed [8]. The present linear trend is attributed to the relatively short corrosion time, the inferior corrosion resistance of aluminum alloy 7075-T7651 (relative to aluminum alloy 2024), as well as the smaller specimen thickness. It was also observed that localized corrosion promoted initiation of multiple cracks, and the presence of the pits causing stress concentration greatly accelerated crack initiation and promoted crack growth. These experimental results are in agreement with the finding reported previously on the fatigue failure of pre-corroded aluminum alloys 2024 and 7050 [18, 22]. Although the fact that prior localized corrosion causes the degradation of mechanical properties of aluminum alloy, and promotes crack initiation though stress concentration is well known, there is still a lack of quantitative analysis of when and where these cracks initiate, and how they evolve and interact leading to final failure, especially for different levels of prior corrosion. One important contribution in this paper is to visually show specific temporal-spatial experimental information about damage evolution and crack propagation with different levels of prior corrosion, associated with loading curves and fracture morphology, which has not been adequately discussed before. The loading curves represent the mechanical response of the whole specimen, while the DIC strain maps give more detailed local characterization of strain concentration, damage evolution, crack initiation and propagation, as well as crack interaction. In addition, the shapes and sizes of corrosion pits in the key damage regions were identified from the fracture morphology.

The experimental results visually show that the damage evolution and failure process temporally and spatially differs in the specimens with aggravated corrosion damage, and provide specific and quantitative analysis that prior corrosion affected the strain, location of localized damage, micro-cracking initiation and coalescence, as well as cracking orientation and propagation. For example, a critical effect of the corrosion damage is to accentuate local strain concentration at maximum load. It could be observed that the 4 hrs and the 6 hrs cases increase strain concentration from 1.6 (no corrosion) to 2.0 (4 hrs) and 2.7 (6 hrs), resulting inevitably in reduced ductility. It is also found that the local maximum principal strain at final failure reduces significantly, and proportionally with corrosion duration by 18% (absolute) and 26%, respectively for 4 hrs and 6 hrs. Localized corrosion leads to earlier crack formation. It was observed that cracks form at the peak load when the corrosion damage is more severe, as shown in Fig. 8 (B_3). Although multiple cracks initiated and evolved simultaneously, propagation and coalescence of the main cracks, formed in KDRs, dominated the failure process. For example, some cracks outside KDR II_2 formed before those in KDR II_2 and were larger, e.g. see C_2 in Fig. 7, but these did not propagate with further deformation (see D_2 and E_2 in Fig. 7). This indicates that the locations of key damage region depends on both the local corrosion morphology and local stress conditions.

Based on these experimental observation, the entire damage evolution and failure process of aluminum alloy with prior corrosion damage is illustrated in Fig. 12, including pre-corrosion and tension stages. In the pre-corrosion stage, corrosion pits grow with increasing corrosion time, leading to the evolution of initial corrosion damage. At this stage, the total damage D_{total} can be written as

$$D_{total} = D_{cor} \tag{10}$$

where D_{cor} is the initial corrosion damage. In the tension stage, initial corrosion damage cause the degradation of mechanical properties. The total damage further accumulates by growth of mechanical damage under loading, giving

$$D_{total} = D_{cor} + D_{mech} \tag{11}$$

in which D_{mech} is the plastically-induced mechanical damage.

Fig. 12 also contains a schematic representation of the proposed interaction between the corrosion and mechanical damage processes. The initial status of the pre-corroded material at zero loading is shown in Fig. 12 (b). The material contains some impurity and second phase particles, as well as some localized corrosion damage. Under the tensile stress field, damage growth occurs at the edge of some corrosion damage sites in multiple regions; meanwhile voids nucleate at impurities and second phase particles by either interface decohesion or particle cracking. As shown in the Fig. 12 (c) and (d), corrosion defects and voids grow further depending on the local stress condition and, finally, these forms of damage coalesce when they reach a critical size, leading to final fracture. The fracture is controlled by the damage evolution of key (corrosion) damage regions, as characterized by the experimental results.

4. MODELLING

Based on the discussion on damage evolution, the corrosion-affected mechanical response of whole specimen in uniaxial tension test can be approximately modelled based on damage mechanics. Similar to un-corroded specimen described in section 3.2, tensile curve of pre-corrosion specimen could also be roughly divided into elastic, plastic, and soften stages; it is also assumed that plasticity-induced mechanical damage initiates when strain reaches the ultimate strain. In the elastic stage, initial corrosion damage lead to the degradation of elasticity modulus. In the plastic stage, initial corrosion damage caused the degradation of hardening parameters. In the softening (damage progression) stage, total damage was further accumulated by initial corrosion damage and plastically-induced mechanical damage then cause the stress softening. Thus, when the initial corrosion damage is determined, the corrosion-affected tensile curves could be simulated by introducing the initial corrosion damage D_{cor} to the identified material parameters from the un-corroded specimen in different stages.

Since the degradation of apparent elasticity modulus approximately proportionally to pre-corrosion exposure duration in our tests, the initial corrosion damage D_{cor} can be estimated as

$$D_{cor} = 1 - \frac{\tilde{E}}{E} \approx k_1 t \tag{12}$$

where $\tilde{E}$ represents the apparent elasticity modulus of pre-corroded material, k_1 is a constant to reflect the degradation of apparent elasticity modulus with increasing pre-corrosion duration, calibrated from the measured data $k_1 \approx 0.019$, t is the pre-corrosion time.

After that, the initial corrosion damage was introduced to in different stages, inducing the degradation of

mechanical parameters. For the elastic stage:

$$\tilde{E} = E(1-D_{cor}) \tag{13}$$

For the plastic stage:

$$\tilde{Q} = Q(1-D_{cor}) \tag{14}$$

$$\tilde{\varepsilon}_u = \varepsilon_u(1-k_2 D_{cor}) \tag{15}$$

where $\tilde{Q}$ is the apparent hardening parameter of pre-corroded material, $\tilde{\varepsilon}_u$ is the ultimate strain of pre-corroded material which represents the initiation of damage, k_2 is a constant to reflect the change of ultimate strain with initial corrosion damage, calibrated from the measured data $k_2 \approx 4.47$.

For the softening (damage progression) stage:

$$D_{total} = D_{cor} + a_1\left[1-\frac{\left(\frac{\tilde{\varepsilon}_p}{\tilde{\varepsilon}_{pD}}\right)}{y_1}\right]^{x_1} + a_2\left[1-\frac{\left(\frac{\tilde{\varepsilon}_p}{\tilde{\varepsilon}_{pD}}\right)}{y_2}\right]^{x_2} \tag{16}$$

$$\tilde{\varepsilon}_R = \varepsilon_R(1-k_3 D_{cor}) \tag{17}$$

where $\tilde{\varepsilon}_p$ represents the plastic strain of pre-corroded material, and $\tilde{\varepsilon}_{pD}$ is the damage threshold plastic strain of pre-corroded material. k_3 is a calibrated constant to reflect the change of rupture strain as initial corrosion damage; in this work $k_3 \approx 2.74$.

A flowchart for the combined corrosion-mechanical damage model is shown in Fig. 13. Based on Eqs. 12 to 17, the stress-strain curves for different pre-corrosion times were determined. Fig. 14 shows the comparison of the model results with the experimental results, for the three different corrosion conditions. It is clear that the present method can describe the mechanical response considering the corrosion-enhanced damage evolution.

The increased understanding and corrosion-mechanical models presented in this paper will contribute directly to the development of next generation methodologies for corrosion and safety management, to ensure increased flight safety and decreased maintenance costs. Crack initiation and propagation originated for the key damage regions will be further discussed in future work. For example, finite element analysis of three dimensional model pits in NiCrMoV disc steel indicated that strain is a maximum on the pit wall just below the pit mouth [19]. The cellular automata finite element method has been used to illustrate the stress contours around a developing pit in X65 steel [45]. These methods are beneficial to develop a model considering local stress and corrosion morphology.

5. CONCLUSIONS

Uniaxial tension tests have been conducted on 7050-T7651 aluminum alloy exposed to EXCO solution for different short-term durations. The effect of the associated corrosion on damage evolution and crack propagation for the aluminum alloy was experimentally characterized using DIC and SEM. It is concluded

that:

(1) The combined analysis techniques of tensile stress-strain response, full-field strain mapping by DIC and SEM-based fracture morphology form an effective combination to characterize damage evolution and crack propagation in pre-corroded aluminum alloy.

(2) The no-corrosion case has been used to identify threshold strains for damage initiation and cracking and these have been adopted to successfully identify damage evolution in the corroded cases, including the key milestones of damage localization, crack initiation and crack propagation leading to the final fracture, from the full-field DIC inhomogeneous strain distributions.

(3) Corresponding to the proportional degradation of apparent stiffness, strength and ductility, the damage evolution and failure process temporally and spatially differed in specimens with aggravated corrosion damage. Quantitative analysis on the effects of prior corrosion on load, strain, location of localized damage, micro-cracking initiation and coalescence, as well as cracking orientation and propagation, was presented. For the largest corrosion duration, cracks were shown to occur as early as the peak load. Although multiple micro-cracks in some diffuse regions evolved simultaneously, the propagation and coalescence of cracks originating from identified key damage regions resulted in the final failure, revealing that the key damage regions dominated the damage evolution and failure process.

(4) A damage mechanics model has been developed to simulate the mechanical response of non-corroded and pre-corroded aluminum alloy, including the effect of increasing exposure time. The modelling results show close correlation with the measured responses.

Acknowledgements

This research was supported by the National Natural Science Foundation of China (NSFC, Grant Nos. 11502285 and 11472298), the Science Foundation Ireland (SFI, Grant No. 14/IA/2604) and the Fundamental Research Funds for the Central Universities (FRFCU, Grant No. 3122014H006).

References

1. Dursun T, Soutis C (2014) Recent developments in advanced aircraft aluminium alloys. *Mater Design (1980-2015)*. **56**: 862-871.
2. Hu P, Meng QC, Hu WP, Shen F, Zhan ZX, Sun LL (2016) A continuum damage mechanics approach coupled with an improved pit evolution model for the corrosion fatigue of aluminum alloy. *Corros Sci*. **113**: 78-90.
3. Huang YF, Ye XB, Hu BR, Chen LJ (2016) Equivalent crack size model for pre-corrosion fatigue life prediction of aluminum alloy 7075-T6. *Int J Fatigue*. **88**: 217-226.
4. Molent L (2015) Managing airframe fatigue from corrosion pits – A proposal. *Eng Fract Mech*. **137**: 12-25.
5. DuQuesnay DL, Underhill PR, Britt HJ (2003) Fatigue crack growth from corrosion damage in 7075-T6511 aluminium alloy under aircraft loading. *Int J Fatigue*. **25**: 371-377.
6. Crawford BR, Loader C, Ward AR, et al. (2005) The EIFS distribution for anodized and pre-corroded 7010-T7651 under constant amplitude loading. *Fatigue Fract Eng M*. **28**: 795-808.
7. Pantelakis S, Setsika D, Chamos A, Zervaki A (2016) Corrosion damage evolution of the aircraft aluminum alloy 2024 T3. *Int J Struct Integr*. **7**: 25-46.
8. Alexopoulos ND, Papanikos P (2008) Experimental and theoretical studies of corrosion-induced mechanical properties degradation of aircraft 2024 aluminum alloy. *Mat Sci Eng A-Struct*. **498**: 248-257.
9. Sabelkin V, Misak HE, Perel VY, Mall S (2016) Crack Initiation from Corrosion Pit in Three Aluminum Alloys Under Ambient and Saltwater Environments. *J Mater Eng Perform*. **25**: 1631-1642.
10. Li X-D, Wang X-S, Ren H-H, Chen Y-L, Mu Z-T (2012) Effect of prior corrosion state on the fatigue small cracking behaviour of 6151-T6 aluminum alloy. *Corros Sci*. **55**: 26-33.
11. Weber M, Eason PD, Ozdes H, Tiryakioglu M (2017) The effect of surface corrosion damage on the fatigue life of 6061-T6 aluminum alloy extrusions. *Mat Sci Eng A-Struct*. **690**: 427-432.
12. Chen YJ, Liu CC, Zhou J, Wang XC (2017) Multiaxial fatigue behaviors of 2024-T4 aluminum alloy under different corrosion conditions. *Int J Fatigue*. **98**: 269-278.
13. Burns JT, Larsen JM, Gangloff RP (2012) Effect of initiation feature on microstructure-scale fatigue crack propagation in Al–Zn–Mg–Cu. *Int J Fatigue*. **42**: 104-121.
14. Burns JT, Gupta VK, Agnew SR, Gangloff RP (2013) Effect of low temperature on fatigue crack formation and microstructure-scale propagation in legacy and modern Al–Zn–Mg–Cu alloys. *Int J Fatigue*. **55**: 268-275.
15. McMurtrey MD, Bae D, Burns JT (2017) Fracture mechanics modelling of constant and variable amplitude fatigue behaviour of field corroded 7075-T6511 aluminium. *Fatigue Fract Eng M*. **40**: 605-622.
16. Russo S, Sharp PK, Dhamari R, et al. (2009) The influence of the environment and corrosion on the structural integrity of aircraft materials. *Fatigue Fract Eng M*. **32**: 464-472.
17. Kim S, Burns JT, Gangloff RP (2009) Fatigue crack formation and growth from localized corrosion in Al–Zn–Mg–Cu. *Eng Fract Mech*. **76**: 651-667.
18. van der Walde K, Brockenbrough JR, Craig BA, Hillberry BM (2005) Multiple fatigue crack growth in pre-corroded 2024-T3 aluminum. *Int J Fatigue*. **27**: 1509-1518.
19. Horner DA, Connolly BJ, Zhou S, Crocker L, Turnbull A (2011) Novel images of the evolution of stress corrosion cracks from corrosion pits. *Corros Sci*. **53**: 3466-3485.
20. van der Walde K, Hillberry BM (2007) Initiation and shape development of corrosion-nucleated fatigue cracking. *Int J Fatigue*. **29**: 1269-1281.
21. Joshi G, Mall S (2017) Crack Initiation and Growth from Pre-corroded Pits in Aluminum 7075-T6 Under Laboratory Air and Salt Water Environments. *J Mater Eng Perform*. **26**: 2293-2304.
22. Co NEC, Burns JT (2017) Effects of macro-scale corrosion damage feature on fatigue crack initiation and fatigue behavior. *Int J Fatigue*. **103**: 234-247.
23. Turnbull A, Wright L, Crocker L (2010) New insight into the pit-to-crack transition from finite element analysis of the stress and strain distribution around a corrosion pit. *Corros Sci*. **52**: 1492-1498.
24. Cerit M (2013) Numerical investigation on torsional stress concentration factor at the semi elliptical corrosion pit. *Corros Sci*. **67**: 225-232.
25. Amiri M, Arcari A, Airoldi L, Naderi M, Iyyer N (2015) A continuum damage mechanics model for pit-to-crack transition in AA2024-T3. *Corros Sci*. **98**: 678-687.
26. Sutton MA, Orteu JJ, Schreier HW (2009) *Image correlation for shape, motion and deformation measurements: basic concepts, theory and applications*. Springer.
27. Pan B, Qian K, Xie H, Asundi A (2009) Two-dimensional digital image correlation for in-plane displacement and strain measurement: a review. *Meas Sci Technol*. **20**: 062001.

28. Kang Y-L, Zhang Z-F, Wang H-W, Qin Q-H (2005) Experimental investigations of the effect of thickness on fracture toughness of metallic foils. *Mat Sci Eng A-Struct*. **394**: 312-319.
29. Jiang R, Pierron F, Octaviani S, Reed PAS (2017) Characterisation of strain localisation processes during fatigue crack initiation and early crack propagation by SEM-DIC in an advanced disc alloy. *Mat Sci Eng A-Struct*. **699**: 128-144.
30. Ren C, Zhang X, Ji H, Zhan N, Qiao Z (2017) Effect of banded morphology and grain size on the tensile behavior of acicular ferrite in HSLA steel. *Mat Sci Eng A-Struct*. **705**: 394-401.
31. Ning ZL, Liang WZ, Kang ZJ, Sun HC, Sun JF (2017) Strain-field evolution in a CuZr-based bulk metallic glass composite during tensile deformation. *Mat Sci Eng A-Struct*. **697**: 233-237.
32. Song H, Zhang H, Fu D, Zhang Q (2016) Experimental analysis and characterization of damage evolution in rock under cyclic loading. *Int J Rock Mech Min*. **88**: 157-164.
33. Bolivar J, Frégonèse M, Réthoré J, Duret-Thual C, Combrade P (2017) Evaluation of multiple stress corrosion crack interactions by in-situ Digital Image Correlation. *Corros Sci*. **128**: 120-129.
34. Kovac J, Alaux C, Marrow TJ, Govekar E, Legat A (2010) Correlations of electrochemical noise, acoustic emission and complementary monitoring techniques during intergranular stress-corrosion cracking of austenitic stainless steel. *Corros Sci*. **52**: 2015-2025.
35. Duff JA, Marrow TJ (2013) In situ observation of short fatigue crack propagation in oxygenated water at elevated temperature and pressure. *Corros Sci*. **68**: 34-43.
36. Lemaitre J, Chaboche J-L (1994) *Mechanics of solid materials*. Cambridge university press.
37. Lemaitre J, Desmorat R (2005) *Engineering damage mechanics: ductile, creep, fatigue and brittle failures*. Springer Science & Business Media.
38. Sankaran KK, Perez R, Jata KV (2001) Effects of pitting corrosion on the fatigue behavior of aluminum alloy 7075-T6: modeling and experimental studies. *Mat Sci Eng A-Struct*. **297**: 223-229.
39. Standard A (2001) G34-01. *Standard Test Method for Exfoliation Corrosion Susceptibility in 2XXX and 7XXX Series Al Alloys*.
40. Hart E (1967) Theory of the tensile test. *Acta Metall*. **15**: 351-355.
41. Jonas J, Holt R, Coleman C (1976) Plastic stability in tension and compression. *Acta metall*. **24**: 911-918.
42. Considere A (1885) Use of the iron and steel in buildings. *Ann Des Ponts Chaussees*. **9**: 574-575.
43. Dunne F, Petrinic N (2005) *Introduction to computational plasticity*. Oxford University Press on Demand.
44. Turnbull A, McCartney LN, Zhou S (2006) A model to predict the evolution of pitting corrosion and the pit-to-crack transition incorporating statistically distributed input parameters. *Corros Sci*. **48**: 2084-2105.
45. Larrosa N, Akid R, Ainsworth R (2017) Corrosion-fatigue: a review of damage tolerance models. *Int Mater Rev*. 1-26.

Figure Captions

Fig. 1. Microstructure of 0.8mm thick 7050-T7651 specimen.

Fig. 2. Corrosion morphology of 7075-T7651 aluminum alloy along the L-T direction exposed to EXCO solution for 0, 4 and 6 hours.

Fig. 3. (a) Schematic diagram of specimen, (b) measured loading curves for specimens in uniaxial tension tests for different pre-corrosion times of 0, 4 and 6 hours.

Fig. 4. Degradation of macro-scale mechanical properties versus exposure time: (a) apparent elasticity modulus, (b) apparent yield stress and apparent ultimate stress, (c) apparent ultimate strain and apparent rupture strain.

Fig. 5. Identification of material parameters and threshold strain of damage and cracking.

Fig. 6. Visualization of deformation, damage evolution and crack propagation in pristine specimen, represented by maximum tensile strain fields shown in the colored images A_1, B_1, C_1, D_1 and E_1, corresponding the loading points A_1-E_1 marked in the stress-strain curve.

Fig. 7. Visualization of deformation, damage evolution and crack propagation in specimen with a pre-corrosion time of 4 hours, represented by maximum tensile strain fields shown in the colored images A_2, B_2, C_2, D_2 and E_2, corresponding the loading points A_2-E_2 marked in the stress-strain curve.

Fig. 8. Visualization of deformation, damage evolution and crack propagation in specimen with a pre-corrosion time of 6 hours, represented by maximum tensile strain fields shown in the colored images A_3, B_3, C_3, D_3 and E_3, corresponding the loading points A_3-E_3 marked in the stress-strain curve.

Fig. 9. Typical SEM fractographs for pristine specimen (a) fracture path, (b) enlarged view of key damage region I_1, (c) enlarged view of key damage region I_2, (d) ductile fracture characteristic.

Fig. 10. Typical SEM fractographs for specimen with a pre-corrosion time of 4 hours (a) fracture path, (b) enlarged view of key damage region II_1, (c) enlarged view of key damage region II_2, (d) embrittlement of material.

Fig. 11. Typical SEM fractographs for specimen with a pre-corrosion time of 6 hours (a) fracture path, (b) enlarged view of key damage region III_1, (c) enlarged view of key damage region III_2, (d) inclusion.

Fig. 12. (a) Entire damage evolution process of pre-corrosion aluminum alloy, (b) initial status of material with pre-corrosion damage, (c) growth of corrosion damage and void damage, (d) damage coalescence.

Fig. 13. Flowchart for the combined corrosion-mechanical damage model to simulate tensile response.

Fig. 14. Calculated and experimental stress-strain curves of aluminum alloy 7050-T7651 with corrosion times of 0, 4 and 6 hours.

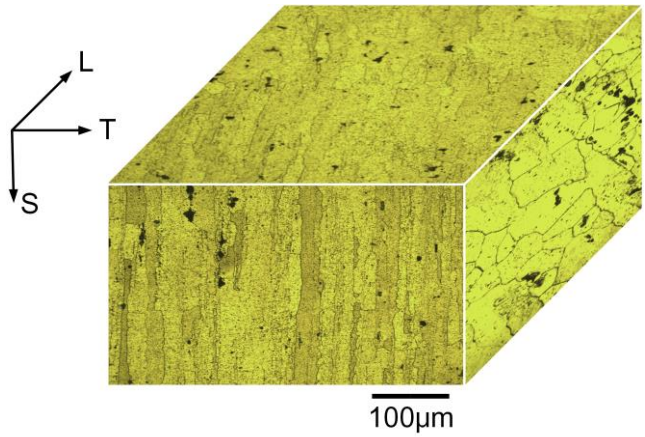

Fig. 1. Microstructure of 0.8mm thick 7050-T7651 specimen.

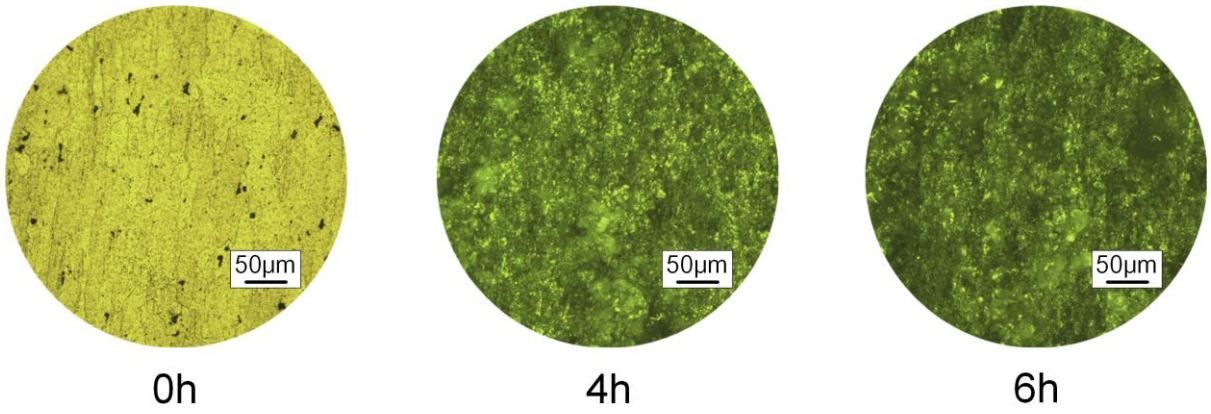

Fig. 2. Corrosion morphology of aluminum alloy 7075-T7651 along the L-T direction exposed to EXCO solution for 0, 4 and 6 hours.

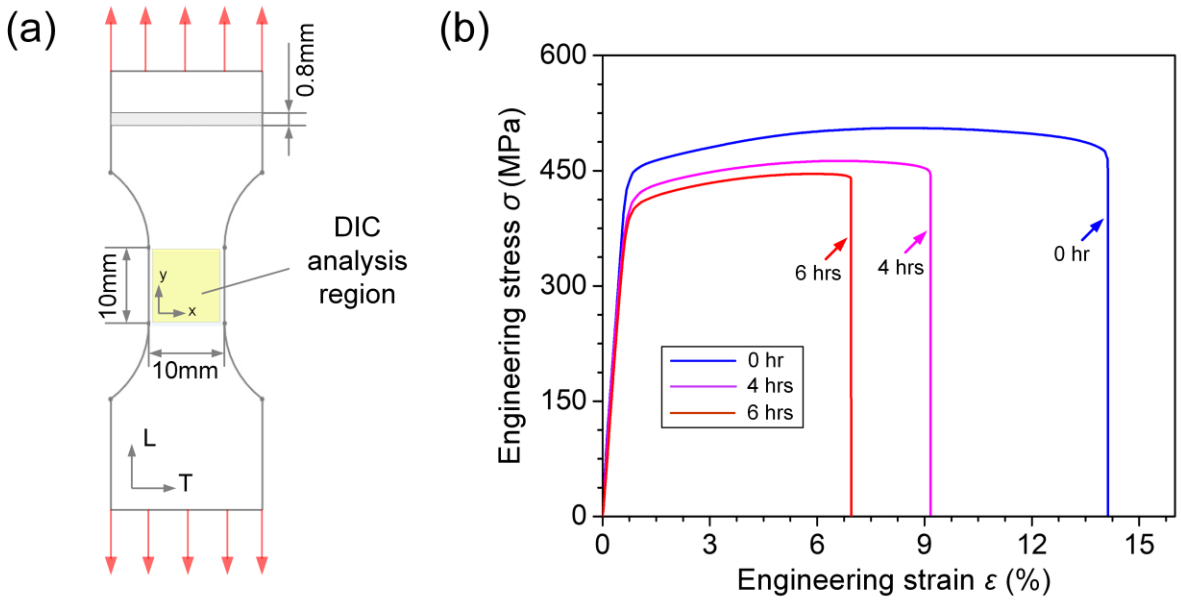

Fig. 3. (a) Schematic diagram of specimen, (b) measured loading curves for specimens in uniaxial tension tests for different pre-corrosion times of 0, 4 and 6 hours.

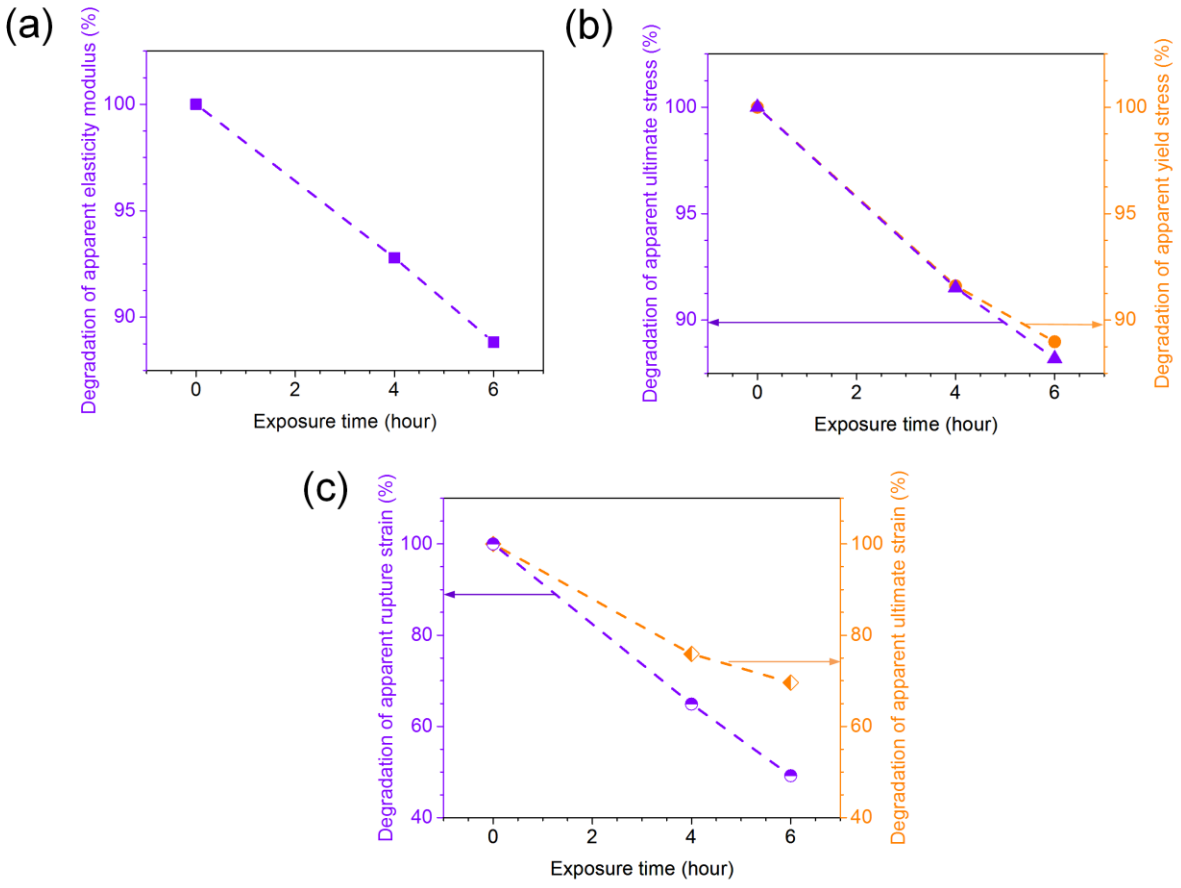

Fig. 4. Degradation of macro-scale mechanical properties versus exposure time: (a) apparent elasticity modulus, (b) apparent yield stress and apparent ultimate stress, (c) apparent ultimate strain and apparent rupture strain.

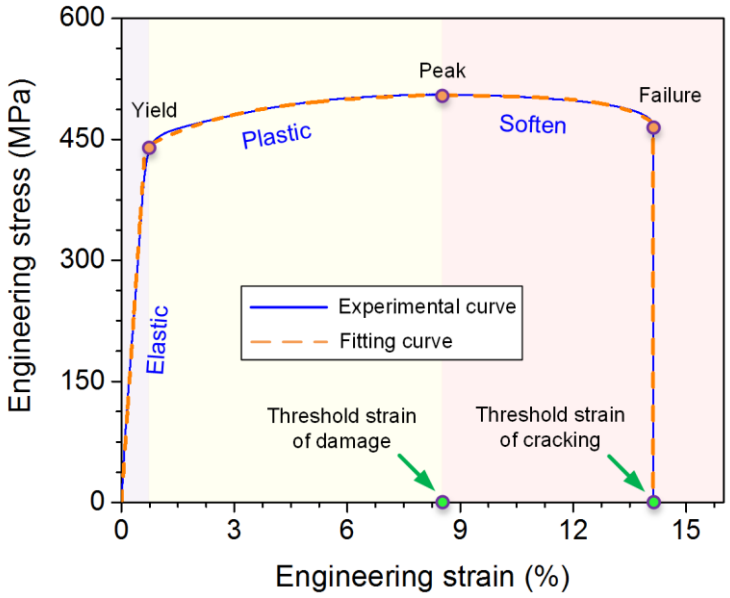

Fig. 5. Identification of material parameters and threshold strain of damage and cracking.

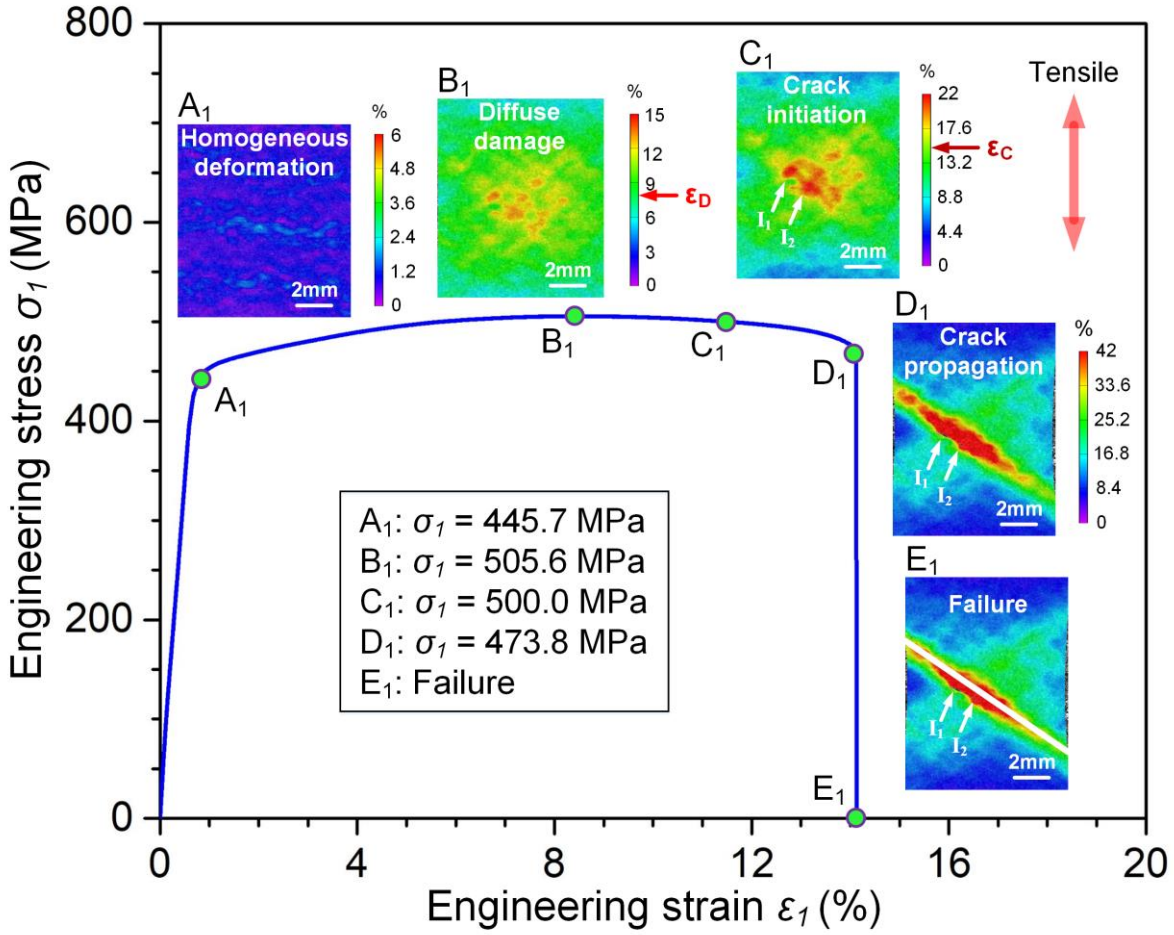

Fig. 6. Visualization of deformation, damage evolution and crack propagation in pristine specimen, represented by maximum tensile strain fields shown in the colored images A_1, B_1, C_1, D_1 and E_1, corresponding the loading points A_1-E_1 marked in the stress-strain curve.

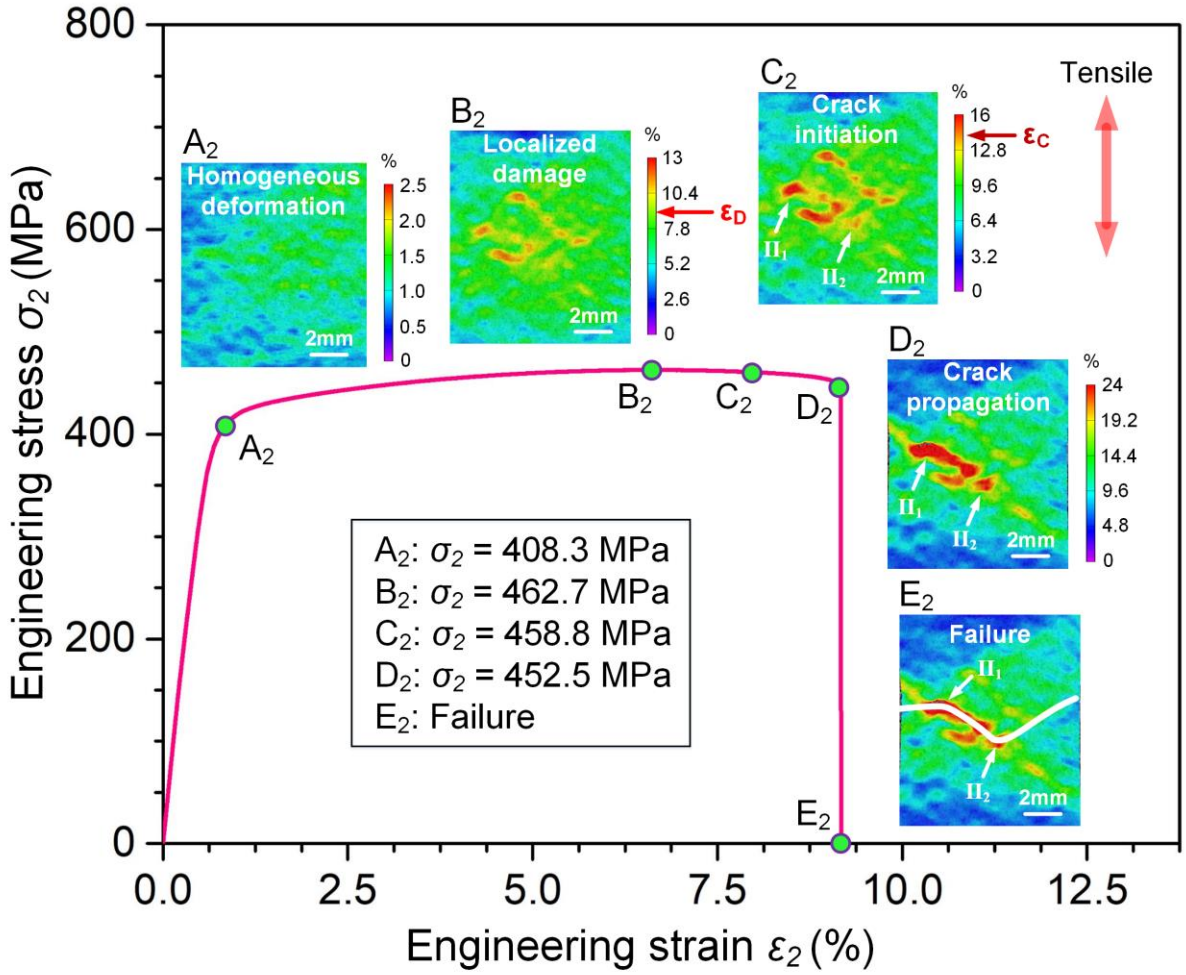

Fig. 7. Visualization of deformation, damage evolution and crack propagation in specimen with a pre-corrosion time of 4 hours, represented by maximum tensile strain fields shown in the colored images A_2, B_2, C_2, D_2 and E_2, corresponding the loading points A_2-E_2 marked in the stress-strain curve.

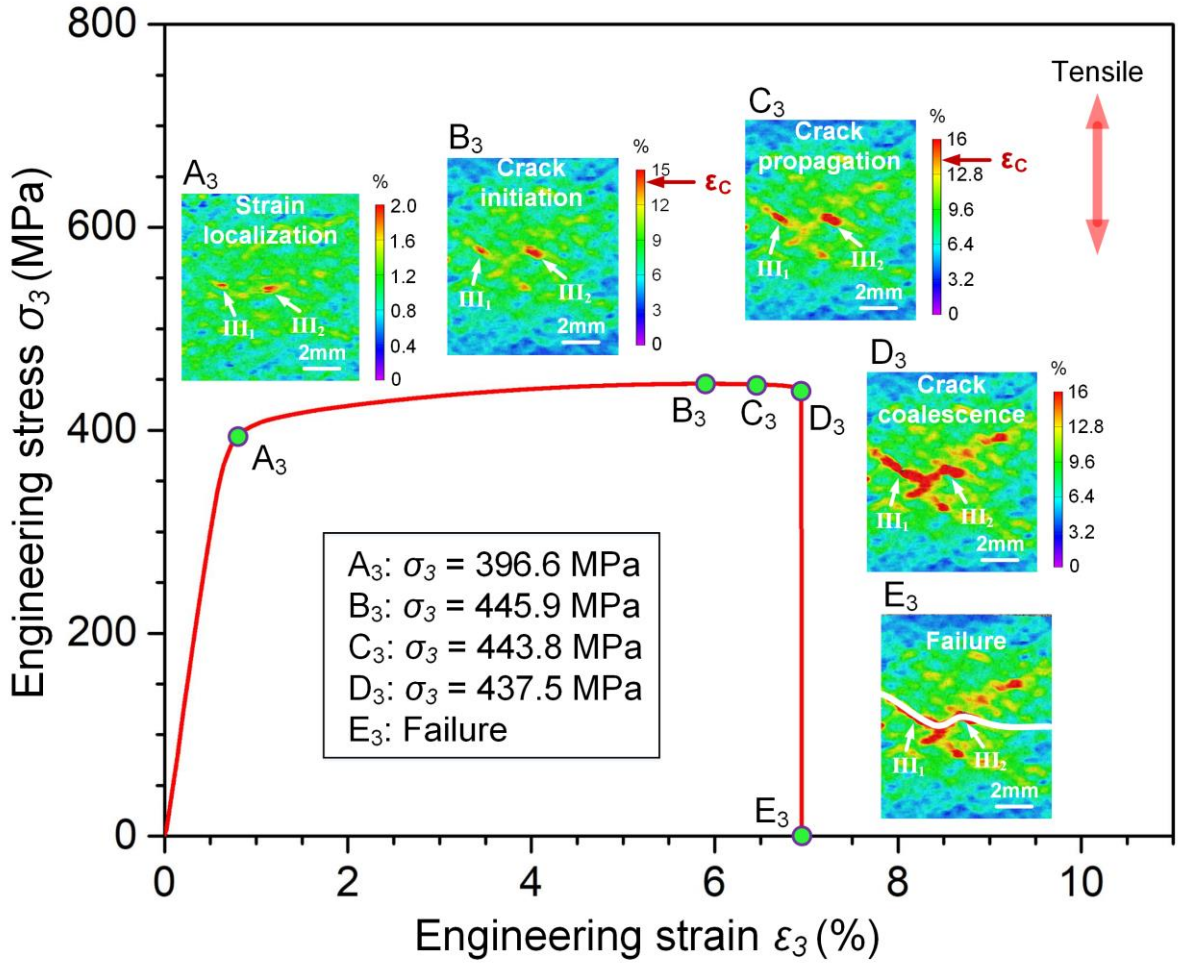

Fig. 8. Visualization of deformation, damage evolution and crack propagation in specimen with a pre-corrosion time of 6 hours, represented by maximum tensile strain fields shown in the colored images A_3, B_3, C_3, D_3 and E_3, corresponding the loading points A_3-E_3 marked in the stress-strain curve.

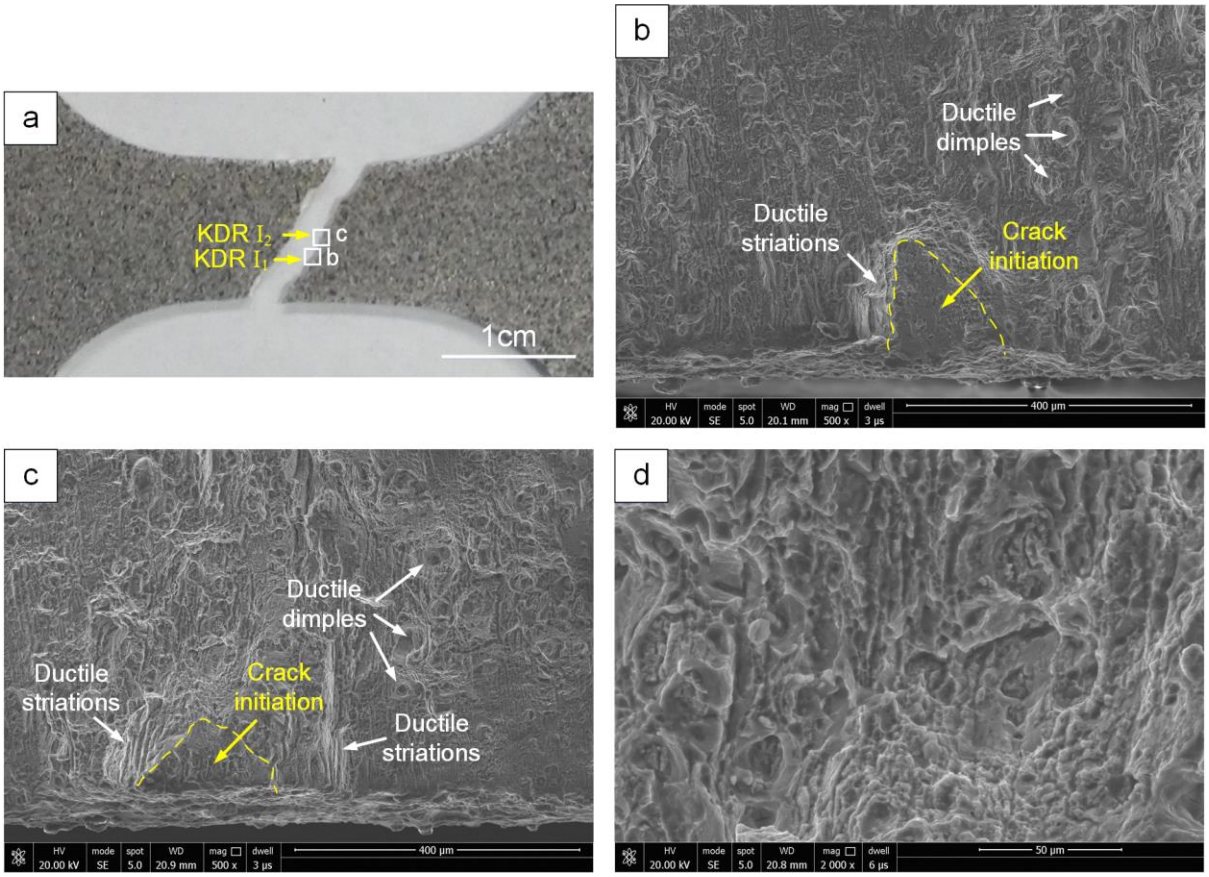

Fig. 9. Typical SEM fractographs for pristine specimen (a) fracture path, (b) enlarged view of key damage region I_1, (c) enlarged view of key damage region I_2, (d) ductile fracture characteristic.

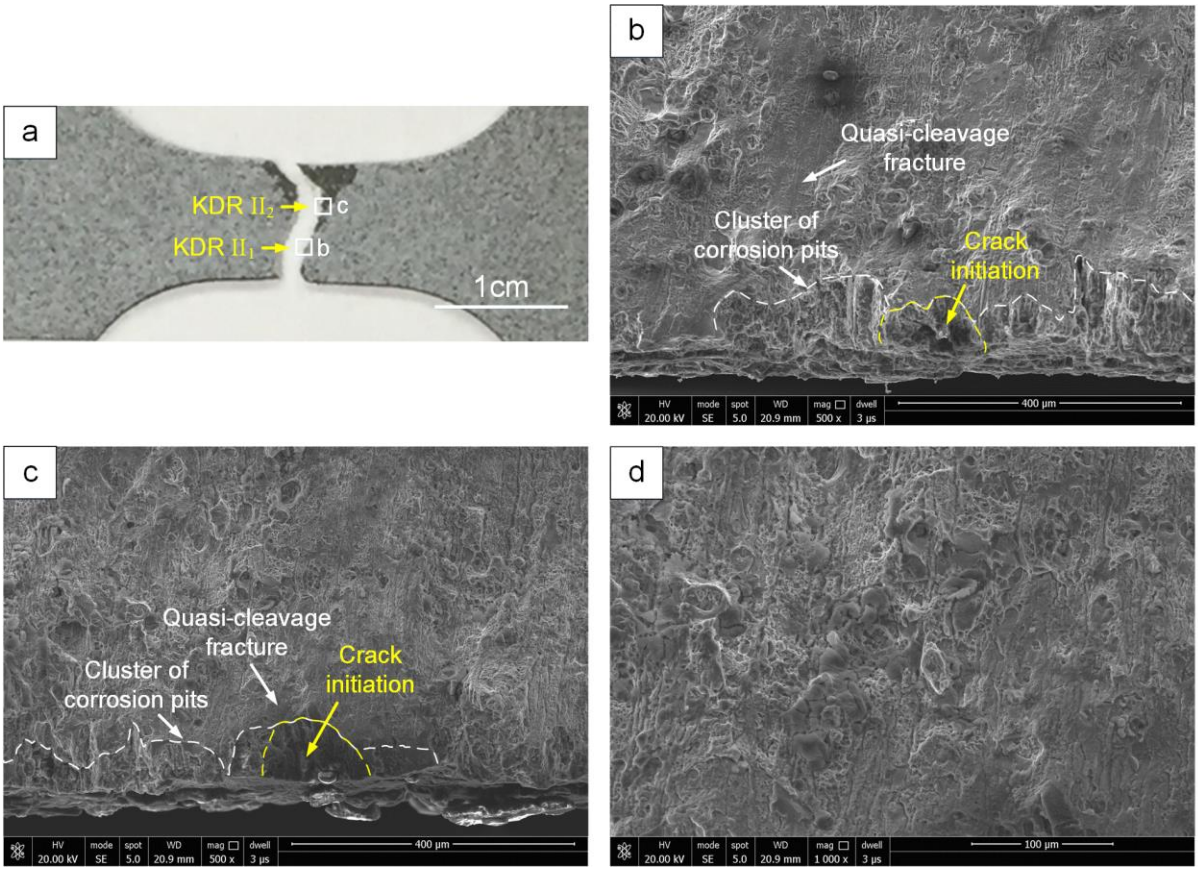

Fig. 10. Typical SEM fractographs for specimen with a pre-corrosion time of 4 hours (a) fracture path, (b) enlarged view of key damage region II_1, (c) enlarged view of key damage region II_2, (d) embrittlement of material.

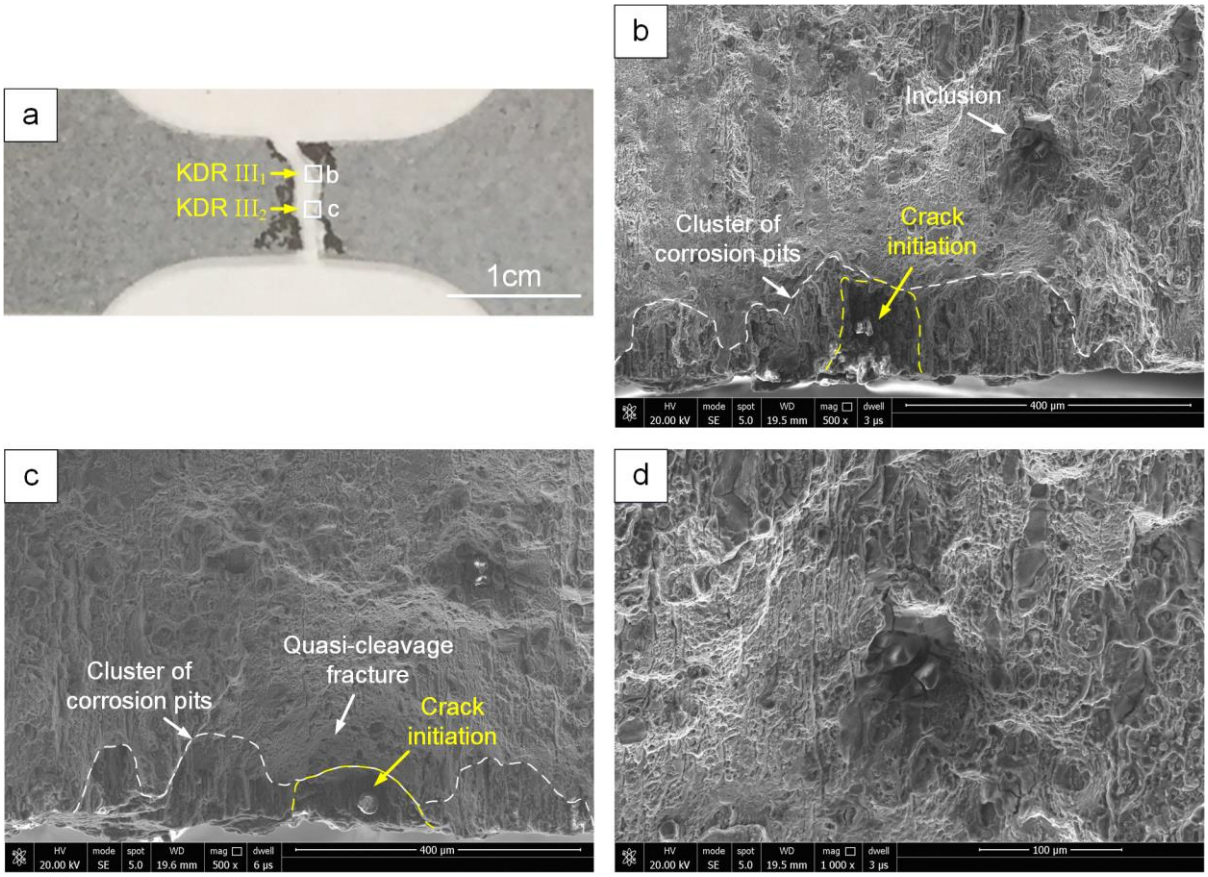

Fig. 11. Typical SEM fractographs for specimen with a pre-corrosion time of 6 hours (a) fracture path, (b) enlarged view of key damage region III_1, (c) enlarged view of key damage region III_2, (d) inclusion.

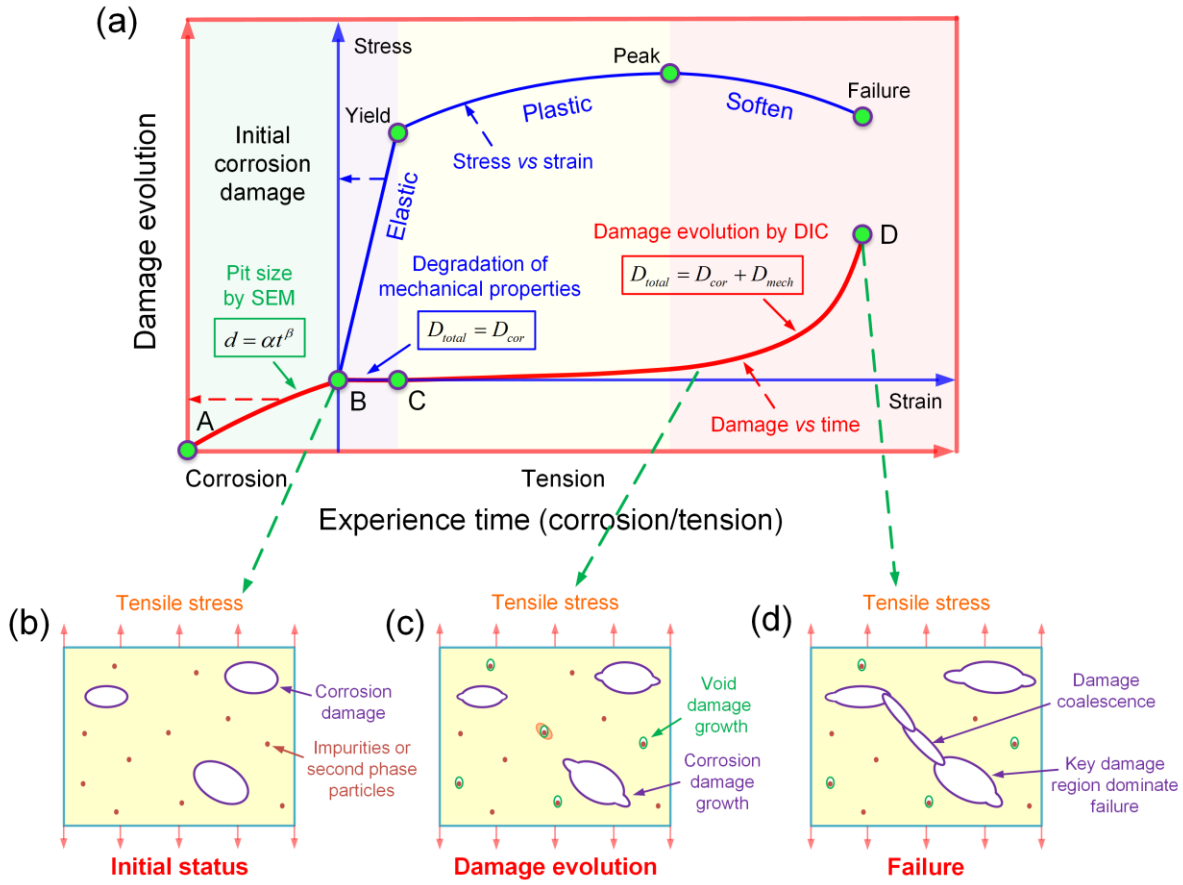

Fig. 12. (a) Entire damage evolution process of pre-corrosion aluminum alloy, (b) initial status of material with pre-corrosion damage, (c) growth of corrosion damage and void damage, (d) damage coalescence.

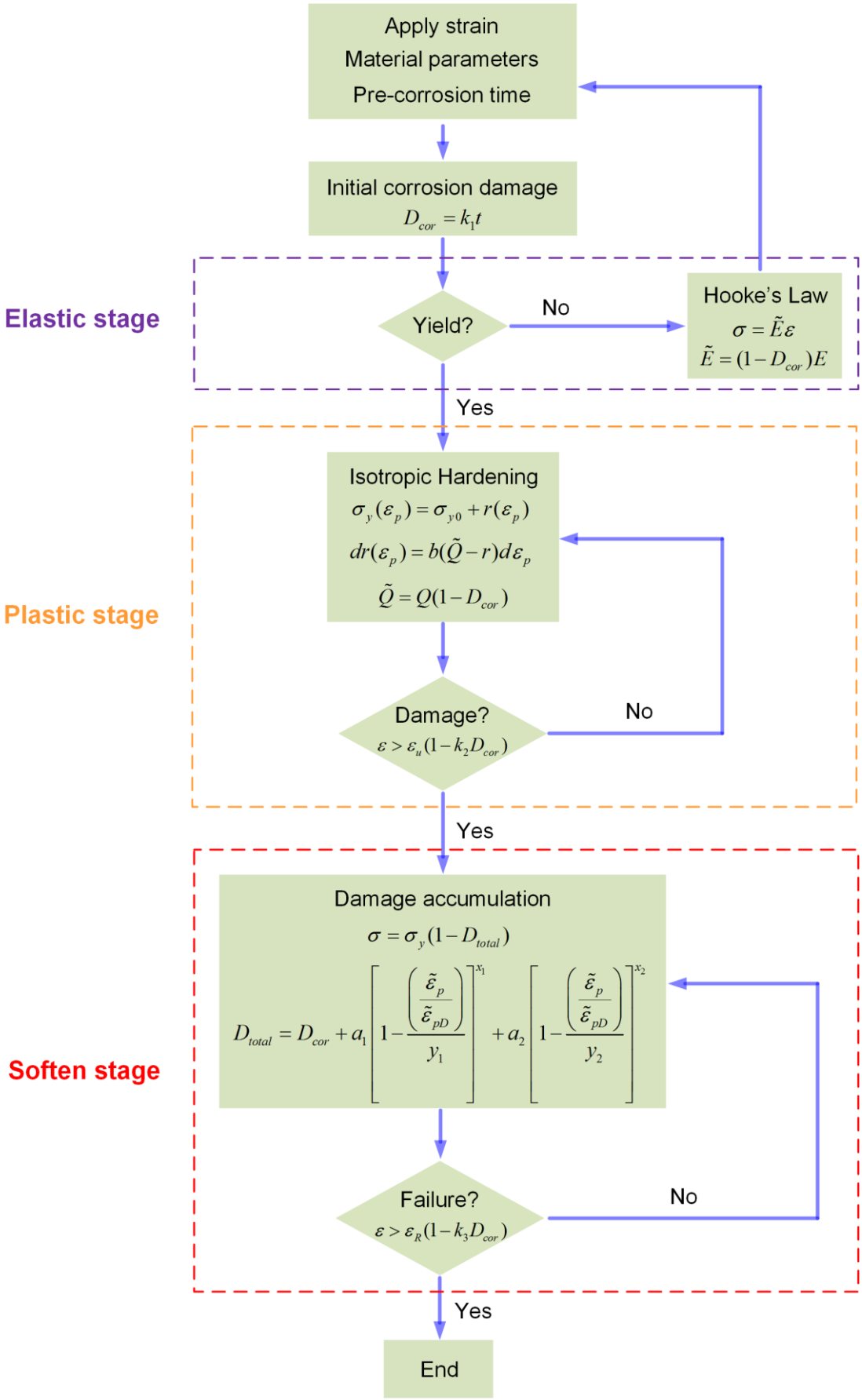

Fig. 13. Flowchart for the combined corrosion-mechanical damage model to simulate tensile response.

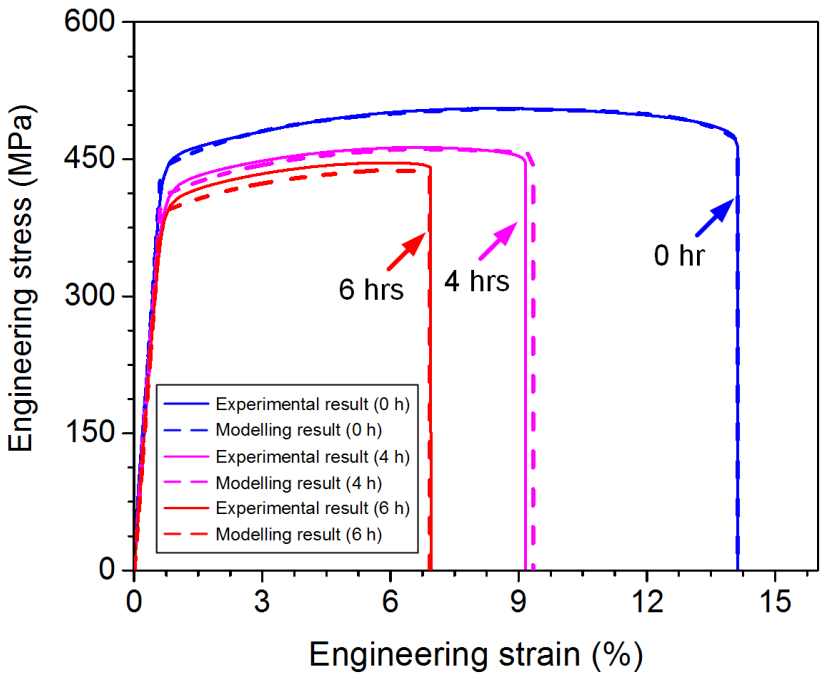

Fig. 14. Calculated and experimental stress-strain curves of aluminum alloy 7050-T7651 with corrosion times of 0, 4 and 6 hours.

Table Captions

Table 1 Mechanical parameters of specimens with different corrosion times.

Table 2 Threshold tensile strains of damage and cracking.

Table 3 Identified damage model parameters for aluminum alloy 7050-T7651.

Table 1 Mechanical parameters of specimens with different corrosion times.

Corrosion exposure T (h)	Apparent elasticity modulus E (GPa)	Apparent yield stress σ_y (MPa)	Apparent ultimate stress σ_u (MPa)	Apparent tensile strain for ultimate stress ε_u (%)	Apparent tensile strain for rupture ε_R (%)
0	70.7	445.7	505.6	8.46	14.13
4	65.6	408.3	462.7	6.42	9.17
6	62.8	396.6	445.9	5.89	6.95

Table 2 Threshold tensile strains of damage and cracking.

Corrosion exposure T (h)	Threshold tensile strain of damage ε_D (%)	Threshold tensile strain of cracking ε_c (%)
0	8.46	14.13

Table 3 Identified hardening and damage parameters for aluminum alloy 7050-T7651.

Q (MPa)	b	a_1	x_1	y_1	a_2	x_2	y_2
63.9	37.6	4.6×10^{-5}	2.6	-7.0	2.3×10^{-4}	2.4	22.1